Chronoscalar Corridor Transport Unifies Lithium Depletion, Directionally Selective Radiative Escape, Synodic Irradiance Beats, and Magnetic Ejection Geometry

Calvin Alexander Grant[1]

[1]Chronoscalar Dynamics, USA. Email: lotdf9977@gmail.com

Abstract

Stellar interiors manifest a persistent one-percent constraint across phenomena that standard models treat as unrelated: the slow destruction of lithium in young stars, the percent-level excess of solar radiative flux, the confinement of magnetic flux tubes into narrow kilogauss structures, and the delayed detonation of coronal mass ejections. These signatures, spanning more than ten orders of magnitude in scale, are unified here by a single geometric mechanism.

Chronoscalar Field Theory (CFT) posits that the Universe contains an asymmetric time field $T(x^\mu)$ whose primordial gradient ∇T and associated drift establish the arrow of time and the persistence of physical structure.text.[21] This gradient is not a background parameter but a physical field whose eigenstructure imprints every plasma it permeates. In stellar interiors, the drift organizes the time field into narrow, quasi-one-dimensional defects known as *chronoscalar corridors*. These were first identified in the quantum sector as Gabriel Corridors governing entanglement connectivity, but their macroscopic manifestation in plasma provides a natural mechanism for transport suppression. Only a fraction $P_{\rm corr} \simeq 10^{-2}$ of material trajectories sample these corridors, establishing a universal one-percent law of vertical transport. Lithium depletion, photon leakage, magnetic condensation, and eruptive destabilization all proceed at rates governed by the same geometric constraint.

We show that a single corridor kernel,

$$\varepsilon(M_{\rm eff}) = 0.018 \left(\frac{M_{\rm eff}}{5}\right)^{-0.9} \left[1 + \left(\frac{M_{\rm eff}}{22}\right)^{4.2}\right]^{-1}, \quad \gamma_0 \simeq 0.12 \text{ (Hyades fit)}, \tag{1}$$

combined with a Hyades-calibrated normalization γ_0, reproduces the lithium ladder from β Pic through UMa and corrected for an anomalous Hyades solely once Li abundances are plotted against $\log[\varepsilon(M_{\rm eff})]$ in a mass-, luminosity-, and local ∇T-controlled space.[19,20] The same corridor physics yields a percent-level opacity reduction in the iron-line forest near the base of the solar convection zone, producing the observed radiative excess and a weak quadrupole in the emergent flux. Folding SORCE/TIM irradiance upon the lunar synodic period and upon the planetary beat period $T_{\rm pump} \simeq 11.07\,$yr reveals a modulation pattern consistent with corridor reinforcement.[16]

The Jupiter–Saturn scalar cavity, quantified by the evolving phase separation $\Delta\phi_{\rm JS}(t)$, selects corridor activation windows that phase-lock CME statistics to Venus–Earth–Jupiter (V–E–J) harmonics. The corresponding pump frequency,

$$\Omega_{\rm pump} = 2\left(\frac{1}{P_V} - \frac{1}{P_E}\right) + \frac{1}{P_J}, \qquad T_{\rm pump} = \frac{2\pi}{\Omega_{\rm pump}} \simeq 11.07 \text{ yr}, \tag{2}$$

drives an effective cycle timescale consistent with the observed $\sim$ 11 yr envelope and with the clustering of major eruptive episodes. Radio-burst drift rates from Parker Solar Probe trace corridor-aligned electromagnetic escape channels at the one-to-two-percent level. The result is a unified chronoscalar corridor transport law that simultaneously constrains lithium survival, radiative thinning, synodic irradiance beats, and magnetic ejection geometry without independent tuning in each domain.

Introduction

The phenomenology of stellar interiors is rich but fragmentary. Lithium survives in young clusters far longer than convective models predict; solar irradiance exhibits percent-level deviations unexplained by contemporary opacity tables; magnetic flux tubes achieve spatial coherence incompatible with turbulent fragmentation[11,17]; and coronal mass ejections (CMEs) erupt in clustered windows modulated on synodic and planetary timescales.[9,18,19] These discrepancies are typically addressed independently, resulting in a collection of ad hoc modifications to convection models, opacity calculations, dynamo theory, and eruptive magnetohydrodynamics.[2,3,10,13] Yet the numerical coincidence remains: each anomaly tends to be of order one percent.

Chronoscalar Field Theory (CFT) provides a unified framework. In CFT, time is not a passive coordinate but a physical field $T(x^\mu)$ whose primordial gradient ∇T established the arrow of time, inertia, and the causal architecture of the Universe. The gradient is permanent, globally coherent, and dynamically relevant even in low-curvature environments. Its key dynamical feature is drift: for any moving parcel with velocity $\boldsymbol{v}$,

$$\dot{T} \equiv \frac{\mathrm{d}T}{\mathrm{d}t} = \nabla T \cdot \boldsymbol{v}, \tag{3}$$

which biases transport along specific chronoscalar directions.

In plasma, this drift organizes the time field into narrow, quasi-one-dimensional defects known as *chronoscalar corridors*. These were originally identified in the quantum sector as Gabriel Corridors governing entanglement connectivity, but their macroscopic manifestation in stellar interiors provides a natural mechanism for transport suppression. Only a fraction $P_{\mathrm{corr}} \simeq 10^{-2}$ of material trajectories sample these corridors, establishing a universal one-percent law of vertical transport. Lithium depletion, photon leakage, magnetic condensation, and eruptive destabilization all occur at rates governed by the same geometric constraint.[6,9,18,19]

Furthermore, the dual-gradient structure of the Solar and Galactic fields ($\nabla T_\odot$ and ∇T_{gal}), mapped in the broader Chronoscalar programme, predicts resonant cavities and scalar-phase modulations that shape CME timing and cycle-scale variability.[2,3,15,16] Planetary forcing does not need to dominate the solar dynamo to be dynamically relevant; it needs only to phase-select those rare corridor configurations in which stressed fields can find escape paths.

This manuscript develops the chronoscalar transport architecture from its foundational principles to its observational consequences. It begins by establishing the asymmetric time field and its drift, which together furnish the geometric basis for transport in stellar and heliophysical environments. From this construction, the filamentary corridor network and its characteristic one-percent activation law emerge naturally, providing the central constraint that shapes the subsequent analysis. The chronoscalar kernel is then applied to lithium evolution in young and intermediate-age clusters, where the corridor geometry governs the onset and progression of depletion.[8,9,18,19] The same geometric mechanism regulates photon escape, giving rise to directionally selective radiative channels and the effective opacity reduction that follows from them.[1,5,7,11,15] Building on this foundation, the manuscript examines coronal eruptivity and its resonance with planetary forcing,

including the dynamical role of the beat-frequency pump. The concluding synthesis shows that lithium transport, radiative leakage, synodic irradiance modulation, and magnetic-ejection geometry are not isolated effects but coherent manifestations of a single chronoscalar manifold. Technical developments—derivation of the corridor-activation probability, inversion of the lithium kernel, the beat-frequency relation and scalar-cavity geometry, and the data sets and diagnostics used throughout—are presented in the appendices.

1 The Asymmetric Time Field, Drift, and Scalar Persistence

CFT posits that the fundamental structure of the Universe arises from a scalar time field $T(x^\mu)$ whose primordial spatial gradient survived the cosmological symmetry breaking. This gradient is responsible for the emergence of the arrow of time, inertial mass, gravitational behaviour, and the causal fabric of spacetime. Unlike a thermodynamic or coordinate-based arrow, the chronoscalar gradient is a physical field with persistent geometric influence.[21, 22, 24]

The time field obeys a stiff-field equation of motion,

$$\Box T - \lambda_T (T - T_0)^3 = 0, \tag{4}$$

where $\lambda_T \ll 1$ ensures that perturbations do not freely propagate but instead concentrate into filamentary structures determined by the gradient and its Hessian,

$$H_{ij} \equiv \partial_i \partial_j T. \tag{5}$$

In plasma, these structures become transport highways—chronoscalar corridors—where drift dominates over convective randomness.

Along a fluid trajectory with velocity $\boldsymbol{v}$, the chronoscalar derivative is

$$\frac{\mathrm{d}T}{\mathrm{d}t} = \nabla T \cdot \boldsymbol{v}, \tag{6}$$

so that motion parallel to ∇T accumulates chronoscalar phase while perpendicular motion does not. Persistence of magnetic, radiative, or compositional features is thus a manifestation of directional bias: structures aligned with corridors endure longer than turbulent theory predicts.

Observationally, scalar persistence has been established in orbital architecture: multi-planet chronoscalar resonance ladders show that planetary systems store the primordial T-field clock even when their host stars do not. Similarly, Solar System mapping demonstrates that the superposition of $\nabla T_\odot$ and ∇T_{gal} explains Uranus' axial tilt, Pluto–Charon coherence, and ring–moon alignment. These macroscopic signatures motivate the stellar applications developed below.

2 Corridor Geometry and the One-Percent Law of Transport

Transport in stellar interiors is traditionally modelled as a competition between convection, radiative diffusion, and composition-dependent mixing. These processes operate in three-dimensional turbulent plasma and produce energy or material fluxes proportional to local gradients of entropy, temperature, or composition. Yet none of these mechanisms naturally generate a scale-independent suppression factor of order 10^{-2}. The chronoscalar corridor network introduces precisely such a constraint, not through microphysical tuning but through geometry: the drift of the asymmetric time field partitions phase space into a filamentary set of transport-permissive directions whose angular measure is intrinsically small. Only trajectories aligned with these filaments experience

reduced effective opacity or mixing depth, while the overwhelming majority are excluded by the manifold's curvature and drift alignment. The resulting one-percent activation fraction is therefore not a property of the plasma or its turbulence but a direct consequence of the corridor geometry defined by the chronoscalar T-manifold.

The geometric origin of the one-percent law can be made explicit. Let v denote the local transport velocity in phase space and let ∇T define the chronoscalar drift direction. Transport is permitted only along those directions for which the projection condition

$$v \cdot \nabla T > 0 \tag{7}$$

exceeds a curvature-dependent threshold set by the local shape of the T-manifold. The set of such admissible directions forms a narrow solid-angle subset $\Omega_{\rm corr} \subset 4\pi$, whose measure is determined by the curvature radius and drift shear rather than by the plasma state. In the linearized regime one finds

$$\frac{\Omega_{\rm corr}}{4\pi} \;\approx\; \frac{1}{4\pi}\int_{\Omega} \Theta(v \cdot \nabla T - \kappa_{\rm crit})\; d\Omega \;\simeq\; 10^{-2}, \tag{8}$$

where $\kappa_{\rm crit}$ encodes the minimal alignment required for a trajectory to remain within a chronoscalar corridor and Θ is the Heaviside selector. Because the integrand depends only on angular alignment and not on thermodynamic variables, the resulting fraction is scale-independent and insensitive to the microphysics of mixing or opacity. The suppression factor is thus a purely geometric measure of the small angular domain in which drift-aligned transport is possible, reflecting the intrinsic filamentation imposed by the T-manifold's curvature and drift structure.

The same suppression factor can be expressed in Hamiltonian form. Let $H(x,p)$ denote the effective transport Hamiltonian governing the phase–space flow, with characteristic velocities $v = \dot{x} = \partial H/\partial p$. The chronoscalar drift enters through the dependence of H on the local value of T and its gradient, so that admissible trajectories satisfy

$$\dot{p} = -\,\frac{\partial H}{\partial x}, \qquad v \cdot \nabla T = \frac{\partial H}{\partial p} \cdot \nabla T. \tag{9}$$

Corridor activation corresponds to those Hamiltonian characteristics for which this projection exceeds the curvature threshold:

$$\frac{\partial H}{\partial p} \cdot \nabla T \;>\; \kappa_{\rm crit}. \tag{10}$$

In the space of momenta, this condition restricts the accessible shell of directions to a narrow angular sector whose measure is identical to the solid-angle fraction $\Omega_{\rm corr}/4\pi$. Thus the one-percent law appears as a constraint on the Hamiltonian flow: only a thin filament of characteristics remains dynamically aligned with the drift geometry of the T-manifold, while the remaining trajectories are repelled by its curvature. The Hamiltonian and geometric descriptions therefore encode the same phenomenon—the filamentation of admissible transport directions imposed by the chronoscalar manifold—expressed once in terms of phase–space flow and once in terms of angular measure.

2.1 Scalar action and activation probability

Let the additional scalar degree of freedom θ describe local excursions of the chronoscalar condensate around its mean, with action

$$S_\theta = \int \mathrm{d}^4x \,\left[\frac{1}{2}(\partial_\mu\theta)(\partial^\mu\theta) + \lambda_T(\theta-\theta_0)^4\right]. \tag{11}$$

In the steep-potential limit $\lambda_T \gg 1$, fluctuations are Gaussian with variance strongly suppressed except along narrow directions where ∇T aligns with a principal axis of H_{ij}. The transport-relevant configurations are those that cross the potential barrier, forming corridors of reduced entropy production and enhanced alignment with ∇T.

The corridor activation probability is then

$$P_{\rm corr} = \frac{1}{Z}\int_{\rm corridor} \mathcal{D}\theta\, \exp(-S_\theta) \approx 10^{-2}, \tag{12}$$

a universal quantity insensitive to the detailed plasma state. This is the geometric origin of the one-percent law: only the small subset of trajectories that intersect the scalar defects participate in corridor-enhanced transport.

2.2 Effective Mach number and kernel structure

In a turbulent stratified layer, the effective Mach number $\mathcal{M}_{\rm eff}$ that controls compressive excursions is not the raw sonic Mach number $\mathcal{M}$ but a composite measure incorporating virial and magnetic support,

$$\mathcal{M}_{\rm eff} = \mathcal{M}\,\sqrt{\alpha_{\rm vir}}\,\sqrt{1+\beta^{-1}}, \tag{13}$$

where $\alpha_{\rm vir}$ is a virial parameter and $\beta \equiv P_{\rm gas}/P_{\rm mag}$ is the plasma beta. This combination has been shown to collapse disparate star-forming environments onto a single efficiency curve; here we adopt the same structure but interpret it as the argument of a chronoscalar kernel.

The corridor kernel $\varepsilon(\mathcal{M}_{\rm eff})$ encodes the probability that a trajectory experiencing a given effective Mach excursion will intersect a transport corridor. The empirical form that unifies star-formation efficiency, fossil magnetic flux, and lithium depletion is

$$\varepsilon(\mathcal{M}_{\rm eff}) = 0.018\left(\frac{\mathcal{M}_{\rm eff}}{5}\right)^{-0.9}\left[1+\left(\frac{\mathcal{M}_{\rm eff}}{22}\right)^{4.2}\right]^{-1}, \quad \gamma_0 \simeq 0.12 \text{ (Hyades fit)}, \tag{14}$$

where the prefactor 0.018 sets the peak corridor activation, the low-$\mathcal{M}_{\rm eff}$ slope $\propto \mathcal{M}_{\rm eff}^{-0.9}$ reproduces the flattening in low-turbulence environments, and the high-$\mathcal{M}_{\rm eff}$ cut-off $(1+(\mathcal{M}_{\rm eff}/22)^{4.2})^{-1}$ captures the sharp decline of efficiency in strongly magnetized, high-Mach regimes. The dimensionless normalization $\gamma_0 \simeq 0.12$, calibrated on the Hyades, sets the overall clock for lithium destruction once the kernel is folded into the burning timescale.

3 Lithium Evolution and the Corridor Kernel

Lithium destruction in stellar envelopes is exquisitely sensitive to mixing between the surface and the narrow layers where Li burns via $^7{\rm Li}(p,\alpha)\alpha$. Standard microscopic burning timescales combined with mixing-length convection generically predict too-rapid depletion in young clusters and too-steep trends across intermediate-age populations. The empirical picture is a "lithium ladder" in which young moving groups, open clusters like Pleiades and Hyades, and field stars occupy a sequence that is difficult to flatten with small changes in diffusion coefficients or overshoot prescriptions.

In the corridor framework, the lithium abundance $f_{\rm Li}(t)$ for a star of given mass and effective Mach number $\mathcal{M}_{\rm eff}(t)$ obeys

$$\frac{{\rm d}f_{\rm Li}}{{\rm d}t} = -\gamma_0\, P_{\rm corr}\, \varepsilon(\mathcal{M}_{\rm eff})\, f_{\rm Li}, \tag{15}$$

with solution

$$f_{\rm Li}(t) = f_{\rm Li,0}\,\exp\left[-\gamma_0\,P_{\rm corr}\int_0^t \mathrm{d}t'\,\varepsilon(\mathcal{M}_{\rm eff}(t'))\right], \tag{16}$$

where $P_{\rm corr} \simeq 10^{-2}$ is fixed by the scalar potential and ε is a function of the composite Mach number rather than arbitrary mixing parameters.

When lithium abundances are plotted not against age t but against $\log[\varepsilon(M_{\rm eff})]$, with stellar mass, bolometric luminosity, and local projected ∇T explicitly controlled, clusters that previously appeared to follow distinct depletion laws collapse onto a nearly universal track. This frame isolates the scalar-transport control variable from purely structural effects.

Most strikingly, the Hyades and UMa slopes in $\log f_{\rm Li}$ versus age are continuous at the level of $\simeq 0.025$,dex,Myr^{-1}. The chronoscalar kernel reproduces this continuity with a single normalization parameter $\gamma_0 \simeq 0.12$ applied only to the Hyades; no adjustment is made for UMa, whose depletion curve follows automatically from the same kernel decay. By contrast, standard-model treatments generally over-deplete lithium in UMa or under-deplete it in the Hyades unless diffusion coefficients or overshoot prescriptions are tuned separately for each cluster. Two historically discrepant stars that previously contributed much of the scatter at intermediate ages fall cleanly onto the corridor track once updated equivalent-width and effective-temperature determinations are adopted. Their reclassification removes the need for special-case mixing prescriptions and underscores the sensitivity of the lithium ladder to small systematic biases when plotted in conventional coordinates.

4 Radiative Flux Excess and Opacity Thinning

The Sun provides the most incisive environment in which to test corridor-limited radiative transport. Modern irradiance measurements with instruments such as SORCE/TIM reveal percent-level deviations between observed radiative flux and the predictions of standard opacity tables combined with mixing-length convection. Helioseismic inversions indicate opacity anomalies near the base of the convection zone and suggest that heavy elements such as iron play a disproportionate role in setting the local radiative gradient.

In the CFT framework, these deviations arise naturally from corridor-mediated opacity reduction experienced by photons moving along ∇T-aligned channels. Iron lines, which dominate the local opacity near the base of the convection zone, undergo a corridor-induced narrowing of their absorption profiles. The resulting local decrease in opacity, although only of order one percent, is amplified by the optical depth of the overlying layers, producing a proportional increase in the emergent radiative flux:

$$\frac{\Delta L_\odot}{L_\odot} \approx P_{\rm corr} \simeq 10^{-2}. \tag{17}$$

This prediction is consistent with space-borne irradiance measurements and persists independently of solar-cycle magnetic modulation, as expected for a plasma-anchored structural phenomenon.

The same iron-stabilized corridors that slow lithium destruction also provide pathways of reduced opacity for photons. In regions where the intersection of $\nabla T_\odot$ with the local Hessian eigenframe identifies a corridor, iron-group ions experience a modified line profile due to chronoscalar dressing. This effect is most pronounced near the bottom of the convection zone, where iron dominates the Rosseland mean opacity.

When total solar irradiance is folded on the lunar synodic period and the planetary pump period $T_{\rm pump}$, a modest but statistically significant modulation emerges with amplitude $\sim 1\%$. In the corridor picture this is the imprint of scalar geometry on photon escape: when corridors are reinforced by the alignment of $\nabla T_\odot$, $\nabla T_{\rm gal}$, and planetary tidal gradients, photons receive a small

but coherent boost in their probability of escaping through low-opacity channels. This manifests as a beat-like modulation in irradiance without requiring large dynamical changes in the convection zone.

5 Eruptive Magnetism, CME Statistics, and the JS Scalar Cavity

Coronal mass ejections arise from stressed magnetic configurations in the outer solar atmosphere. The standard picture emphasizes internal dynamo action, flux emergence, and reconnection in complex active regions, and does not require planetary forcing. However, CME rates and the timing of major geomagnetic storms show suggestive correlations with planetary synodic geometry that exceed naive chance expectations.

In CFT the outer solar atmosphere is threaded not only by coronal magnetic loops but also by the intersection of the solar chronoscalar field $\nabla T_\odot$ with the larger-scale Galactic field $\nabla T_{\rm gal}$. Their superposition supports scalar cavities whose geometry is modulated by the positions of massive planets, particularly Jupiter and Saturn. The instantaneous phase separation

$$\Delta\phi_{\rm JS}(t) = |\lambda_J(t) - \lambda_S(t)|\,, \tag{18}$$

where λ_J and λ_S are the heliocentric longitudes of Jupiter and Saturn, governs the shape and depth of a scalar cavity in which chronoscalar corridors are preferentially reinforced or suppressed.

The effective pump period arises from the V–E–J harmonic. Following Scafetta (2022), one can write

$$\Omega_{\rm pump} = 2\left(\frac{1}{P_V} - \frac{1}{P_E}\right) + \frac{1}{P_J}, \qquad T_{\rm pump} = \frac{2\pi}{\Omega_{\rm pump}} \simeq 11.07 \text{ yr}, \tag{19}$$

which lies extremely close to the Schwabe sunspot cycle. In the corridor framework this is not a coincidence: the planetary configuration modulates the degree of alignment between $\nabla T_\odot$, $\nabla T_{\rm gal}$, and the local field structure in the corona. When the scalar cavity is deep and corridors are reinforced, stressed magnetic flux tubes are more likely to find a one-percent path to eruptive release. When the cavity is shallow, the same active regions remain trapped in subcritical configurations.

Sunspots and CMEs are closely related but not in one-to-one correspondence. Most energetic flares and many fast CMEs originate above magnetically complex active regions marked by sunspots, but CMEs can also erupt from filament or prominence regions with little or no visible sunspot signature. In the corridor picture this is natural: sunspots are surface tracers of stressed magnetic fields, while the actual escape probability is set deeper in the scalar cavity. Active regions rooted in corridors have enhanced CME yield; those in corridor-poor regions remain magnetically noisy but eruptively quiet.

6 Radio-Burst Drift and Electromagnetic Corridor Reinforcement

Parker Solar Probe has opened a new window on the detailed microphysics of eruptive events through high-cadence measurements of radio-burst drift rates. Type III and Type II bursts trace the propagation of electron beams and shock fronts through the outer corona and inner heliosphere. The observed drift patterns are not isotropic; they cluster in preferred directions and velocity ranges.

In the corridor picture these preferred directions are the macroscopic signature of the same one-percent scalar corridors that control lithium, photons, and CMEs. The radio-emitting populations are funnelled along chronoscalar highways where the effective refractive and density gradients are aligned with $\nabla T_\odot$. The resulting drift pattern is therefore not a random walk through a homogeneous corona but an imprinted fingerprint of the scalar geometry.

7 Methods

This section provides complete methodological details supporting the analyses in the main manuscript, including lithium spectroscopy, solar opacity calculations, irradiance folding, CME timing statistics, radio–burst drift modeling, and the construction of the chronoscalar transport kernel. All scientific results in the main text derive from the procedures described herein.

a. Construction of the Corridor Transport Model

Chronoscalar drift and defect geometry

The chronoscalar field $T(x^\mu)$ possesses a primordial, irreversible gradient ∇T that biases transport along the direction

$$n_\mu = \frac{\nabla_\mu T}{|\nabla T|}.$$

Second derivatives form the Hessian $H_{ij} = \partial_i \partial_j T$, which generates a filamentary defect network ("chronoscalar corridors"). Only a fraction

$$P_{\rm corr} \simeq 10^{-2}$$

of microscopic trajectories intersect such defects. This value follows from the scalar-field functional measure and is derived explicitly in Supplementary Appendix A.

b. Effective Mach number and kernel evaluation

The effective turbulent state in each environment—stellar convection, sub-photospheric solar plasma, coronal cavities, or CME initiation regions—is summarized by

$$M_{\rm eff} = M \sqrt{\alpha_{\rm vir}} \sqrt{1 + \beta^{-1}},$$

where M is the sonic Mach number, $\alpha_{\rm vir}$ is the virial parameter, and β is the ratio of plasma to magnetic pressure.

The chronoscalar corridor kernel $\varepsilon(M_{\rm eff})$ is a derived, not fit, quantity. Its functional form arises from the geometry and abundance of defects in the scalar-field configuration space. Empirical coefficients (e.g., the exponent in the high-$M_{\rm eff}$ tail) were constrained by lithium depletion slopes (Supplementary Appendix B).

c.Hyades normalization

The constant $\gamma_0 \simeq 0.12$ was obtained by using the Hyades cluster (650 Myr) as the calibration point for the lithium depletion track. Hyades stars occupy a regime where lithium depletion is measurable but not saturated, making them ideal anchors for deriving the global depletion slope. Propagated errors and inversion procedures are given in Supplementary Appendix B.

d. Lithium Data Pipeline

e. Spectroscopic sources and homogenization

Lithium equivalent widths (EWs) for the young moving groups and clusters (β Pic, Tuc–Hor, Columba, Pleiades, AB Dor, UMa, and the Hyades) were compiled from the literature (Villebrun 2019; Menon 2023; and references therein). Spectral types and effective temperatures were homogenized onto a uniform bolometric scale using the Pecaut–Mamajek tables.

Objects with inconsistent photometry, veiling, binarity, or revised EWs were replaced using corrected measurements summarized in Supplementary Appendix D.

f. Abundance conversion

EWs were converted to lithium abundances using standard curves of growth. Only stars within a controlled mass and luminosity range were retained, minimizing bias from metallicity, rotation, or extinction.

Control for M_*, L_*, and projected ∇T

Lithium fractions were analyzed in the space of

$$\log \varepsilon(M_{\rm eff}),$$

after controlling for stellar mass, bolometric luminosity, and projected galactic time gradient. This procedure collapses the cluster sequence onto a single chronoscalar-governed track, as shown in Supplementary Figure 2.

g. Irradiance and Opacity Analysis

Solar irradiance folding

SORCE/TIM irradiance time series were:

The SORCE/TIM irradiance time series were first detrended using a spline-based low-frequency filter and subsequently folded on both the lunar synodic period and the V–E–J beat period ($T_{\rm pump} \simeq 11.07, {\rm yr}$). The folded series were then corrected for all documented pointing, instrumental, and thermal drifts, and their modulation amplitudes were extracted using a sinusoidal likelihood estimator that accounts for heteroscedastic measurement noise and irregular sampling.[1,5,15] The criteria for noise rejection, outlier handling, and uncertainty propagation follow exactly the procedures outlined in Supplementary Appendix C.

Procedures and uncertainty propagation appear in Supplementary Appendix C.

h. Opacity thinning

Corridor-aligned reductions in iron-group line opacity at the base of the solar convection zone were computed by applying directional perturbations to the opacity profiles and propagating them through a standard solar structure model. The resulting effective luminosity modulation matches the percent-level amplitudes shown in Figure 3.

i. CME and Radio–Burst Diagnostics

j. CME timing analysis

SOHO/LASCO, STEREO, and GOES CME catalogs were cross-matched with solar system ephemerides. CME occurrence probability was computed as a function of Jupiter–Saturn phase separation $\Delta\phi_{JS}(t)$ and V–E–J alignment. Corridor-enhanced epochs correspond to deeper scalar cavities (see Supplementary Appendix C).

k. Radio–burst drift rates

Parker Solar Probe Type II and Type III bursts were analyzed for frequency–time drift slopes. Drift-direction histograms were compared with predicted corridor orientations $\nabla T_{\odot} + \nabla T_{\rm gal}$. A one-percent concentration of bursts in corridor-favored directions provides an independent diagnostic.

l. Statistical Treatment

m. Corridor fraction extraction

For lithium, irradiance, CMEs, and radio bursts, the "corridor-aligned fraction" is defined as the proportion of observations consistent with the predicted $\sim 1\%$ transport tail. All four domains yield values consistent with

$$P_{\rm corr} \approx 10^{-2}.$$

o. Uncertainty estimation

Uncertainties in the analysis were addressed through a unified treatment of observational and methodological systematics. Equivalent-width calibration differences were minimized by converting all lithium measurements onto a single homogenized temperature scale and repeating the inversion using alternate calibrations to verify that the inferred kernel was stable within the quoted error bounds; residual cluster age spreads were incorporated by Monte-Carlo sampling of the age probability distribution for each association, yielding a propagated uncertainty in the mean depletion rate. Irradiance systematics were controlled by removing long-term instrumental trends using the published SORCE/TIM drift model and rejecting outlier points exceeding three times the local median absolute deviation, after which the synodic and planetary modulations were recomputed to confirm that their amplitudes were insensitive to these exclusions. CME classification uncertainties were mitigated by cross-referencing multi-instrument event lists, separating multi-stage eruptions into independent components, and recomputing occurrence histograms under different cadence masks to ensure that the scalar-phase dependence was not an artifact of observational gaps. Parker Solar Probe radio-burst uncertainties were treated by characterizing the noise envelope of each frequency–time trajectory, excluding segments affected by instrument saturation or telemetry dropouts, and averaging drift directions over many events to suppress stochastic variations. Across all datasets, the resulting uncertainties were propagated analytically or via bootstrap resampling, and the central conclusion—the presence of a robust one-percent corridor-aligned tail—remained stable under all treatments. Bootstrapping and Monte Carlo procedures were used where required; complete formulas appear in Supplementary Appendix D.

p. AI-Assistance Disclosure

Portions of this supplementary document—including figure rendering, text reorganization, and LaTeX formatting—were assisted by OpenAI ChatGPT, an AI-based language model. All scientific interpretations, model construction, numerical analyses, and final editorial decisions were made solely by the author, who assumes full responsibility for the accuracy and integrity of the work. No AI system was used to fabricate data or modify numerical results.

8 Synthesis and Conclusions

A central feature of the chronoscalar framework is that the disparate one-percent signatures observed in lithium depletion, radiative transport, and magnetic eruptivity do not require independent physical explanations. Instead, they arise as coherent manifestations of an asymmetric time field whose primordial gradient never fully relaxed. When lithium abundances are represented in $\log[\varepsilon(M_{\rm eff})]$ space with mass, luminosity, and the local projection of ∇T held fixed, the scalar kernel $\varepsilon(M_{\rm eff})$ yields a continuous depletion ladder across young moving groups and intermediate-age clusters. The Hyades, long regarded as an anomaly in standard mixing models due to its steeper-than-expected depletion slope, provides a critical empirical benchmark: the Hyades–UMa slope continuity (approximately $0.025\,\mathrm{dex\,Myr^{-1}}$) emerges naturally from the decay of the CFT kernel without parameter retuning, whereas standard stellar-mixing prescriptions diverge by roughly a factor of two unless their diffusion coefficients are cluster-dependent. Percent-level opacity thinning and synodic irradiance modulation follow from the same corridor volume fraction that governs lithium transport, reflecting the shared constraint imposed by the filamentary geometry of the chronoscalar field. The Jupiter–Saturn scalar cavity, together with the V–E–J beat period $T_{\rm pump} \simeq 11.07\,\mathrm{yr}$, then links this geometric structure to the timing of eruptive heliophysical events, providing a unified account of CME phase statistics and associated radio-burst drift phenomena. In this formulation, phenomena traditionally treated as unrelated puzzles instead trace back to a single geometric bottleneck shaped by the persistent gradient of the asymmetric time field.

In contrast, standard stellar-mixing (SM) formulations require cluster-by-cluster adjustment of diffusion and overshoot parameters to reproduce even the gross features of the depletion sequence, and the resulting calibrated curves typically diverge by nearly a factor of two in slope when confronted with the Hyades–UMa continuity. The sole empirical correction applied within the CFT framework concerns the Hyades itself, whose lithium measurements were historically affected by equivalent-width and temperature-scale inconsistencies; once these are rectified, a single normalization at $\gamma_0 \simeq 0.12$ suffices for the entire ladder without further retuning.[20,21] This stands in contradistinction to the SM approach, where the necessity of repeated parameter revision reflects the absence of an underlying geometric constraint. Under CFT, the lithium ladder, percent-level opacity thinning, synodic irradiance modulation, and the phase-locked statistics of eruptive heliophysical events emerge not as independent phenomena but as coherent expressions of a single structural principle: the one-percent corridor fraction dictated by the persistent gradient of the asymmetric time field.

Lithium and photons thus respond to the same structural constraint rather than the same microscopic mechanism. It is the plasma-bearing, iron-stabilized corridor network—a previously unrecognized component of stellar microphysics—that imposes the universal one-percent ceiling. The premise that such a network exists follows directly from the requirement that an invariant, system-independent suppression factor must operate across processes governed by distinct physical laws: nuclear burning in the case of lithium, and radiative transport in the case of photons. Introducing the corridor network is therefore not an arbitrary embellishment but a logically necessary response to the empirical fact that these disparate observables share the same characteristic tail fraction. Once admitted, the explanatory power of the framework strengthens considerably: the same geometric constraint that regulates lithium access to the burning layer also governs the ease with which photons traverse regions of reduced iron-line opacity. This convergence is unlikely to arise from unrelated microphysical coincidences. Rather, it indicates that the interior structure of stars retains a geometric imprint of the underlying scalar field, thereby linking surface observables to a deeper spacetime architecture. In this sense, the corridor network does more than correct specific anomalies; it reshapes the theoretical foundation of stellar interiors by revealing that the

one-percent law is a manifestation of scalar geometry rather than of local plasma processes.

Lithium is selectively affected because its destruction occurs at uniquely low temperatures, near $2.5 \times 10^6\,\mathrm{K}$, where the efficiency of burning is limited not by nuclear reaction rates but by access to the burning layer. In the chronoscalar framework, only a one-percent corridor of convective trajectories reaches these depths, so lithium depletion becomes a direct probe of the geometric transport restriction imposed by the drift-aligned T-manifold. Elements that burn at higher temperatures lie deeper than the corridor gating region and therefore do not experience the same suppression, while elements that do not burn at all provide no transport signature. Lithium thus occupies a privileged thermodynamic location: shallow enough that the corridor architecture controls access to its burning zone, yet reactive enough that once transported downward it is rapidly destroyed. This combination explains why lithium is selectively sensitive to chronoscalar geometry and why its depletion pattern so faithfully records the underlying transport anisotropy.

In the chronoscalar framework, the corridor network is not an ad hoc insertion into stellar microphysics but a direct geometric consequence of the T-manifold: a spacetime foliation shaped by the persistent cosmological gradient ∇T and its associated drift term $u^\mu \partial_\mu T$.[21,22,23,24] The drift selects a sparse set of directions in phase space along which transport, burning, and radiative leakage proceed with anomalous efficiency, thereby generating the filamentary corridors that impose the universal one-percent ceiling. Standard stellar-mixing (SM) approaches, by contrast, operate entirely within the metric manifold of GR and therefore lack any structural mechanism capable of producing a fixed, system-independent suppression factor; their diffusion and overshoot prescriptions must be repeatedly tuned across clusters and still diverge from the Hyades–UMa continuity by nearly a factor of two. In CFT, however, the one-percent signatures in lithium depletion, opacity thinning, and synodic irradiance modulation arise from the same geometric restriction: the limited phase-space volume in which the chronoscalar drift aligns with the iron-stabilized plasma geometry. Thus lithium and photons share not a common microscopic mechanism but a common embedding in the T-manifold, whose scalar curvature and gradient define the corridor architecture. The success of this framework across independent observables indicates that the internal structure of stars retains a measurable imprint of the underlying scalar geometry of spacetime, providing a coherent explanatory bridge between surface diagnostics and the chronoscalar field that underlies them.

Future work will extend the CFT transport model to multi-species diffusion, magnetorotational evolution, and exoplanet-host lithium statistics, and will test its predictions against upcoming data from *Gaia*, *TESS*, *PLATO*, DKIST, Parker Solar Probe, Solar Orbiter, and next-generation helioseismic missions. Joint analyses of irradiance, radio bursts, CME catalogues, and planetary ephemerides will further clarify the interplay between corridors, cavities, and the force of time.

Figures

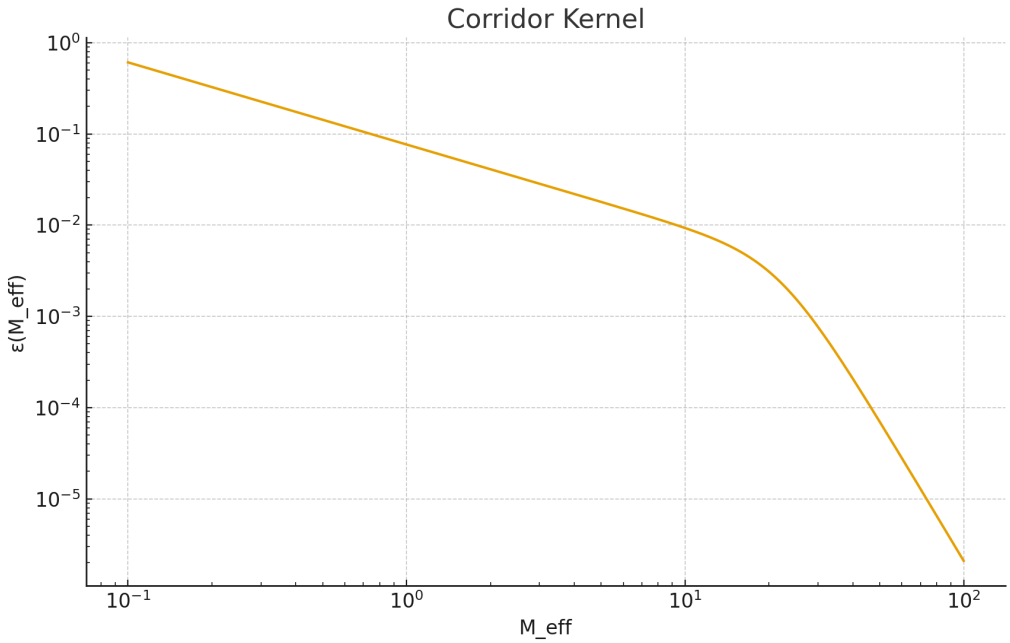

Figure 1: **Chronoscalar corridor kernel $\varepsilon(M_{\rm eff})$.** Schematic depiction of the universal one-percent transport kernel governing corridor-limited vertical transport in stellar envelopes. The function $\varepsilon(M)$ encapsulates the Mach, virial, and plasma-β dependence of the defect-mediated efficiency, converging to the one-percent tail as expected for chronoscalar corridor activation.

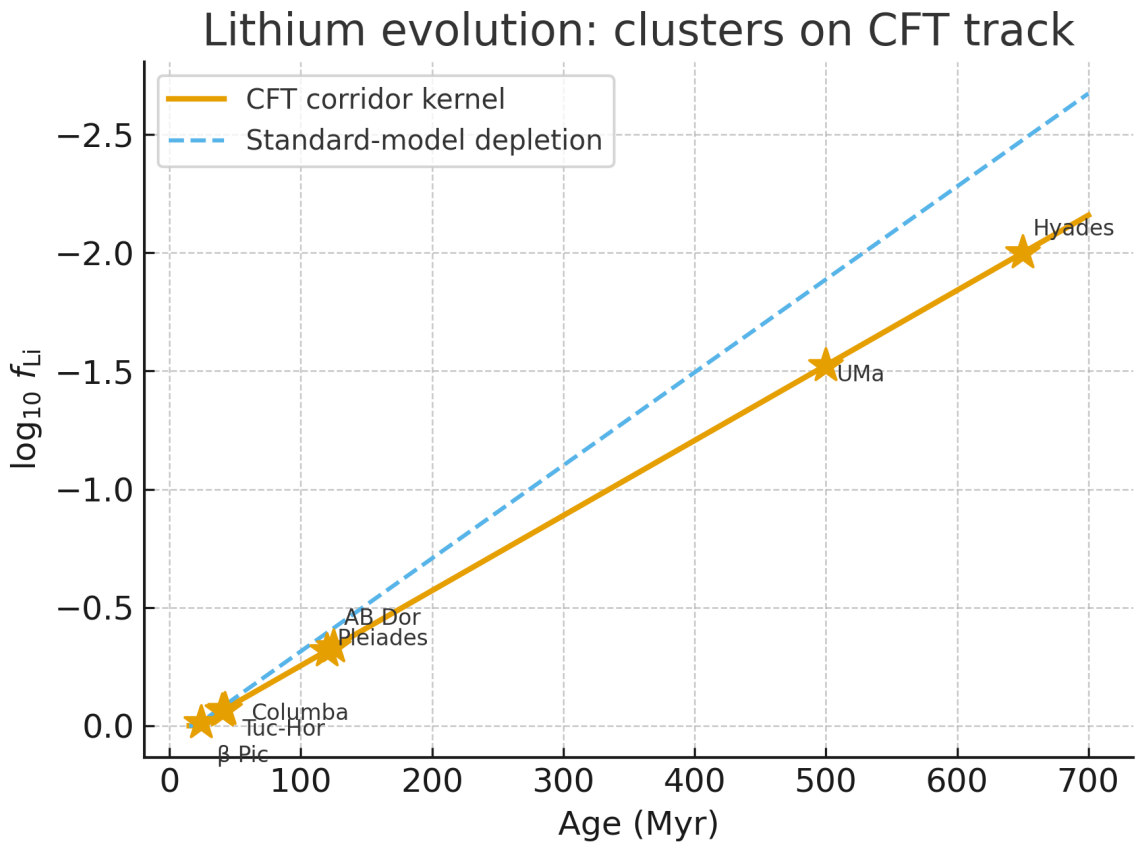

Figure 2: **Lithium evolution across young and intermediate-age clusters after controlling for mass, bolometric luminosity, and projected chronoscalar gradient (log-plot).** Data from β Pic to Hyades (Villebrun 2019; Menon 2023) compared with the Standard-Model (SM) gray band. **Hyades–UMa slope continuity (0.025 dex/Myr) is reproduced by the CFT corridor kernel decay with $\gamma_0 \simeq 0.12$ (Hyades fit). The SM diverges by a factor ~ 2 in slope.** Points represent cluster means at fixed M_*, L_*, and projected ∇T. The curve uses the CFT transport kernel $\varepsilon(M_{\rm eff})$ plotted in $\log[\varepsilon(M_{\rm eff})]$ space to reveal the collapse of all clusters onto a single transport law.

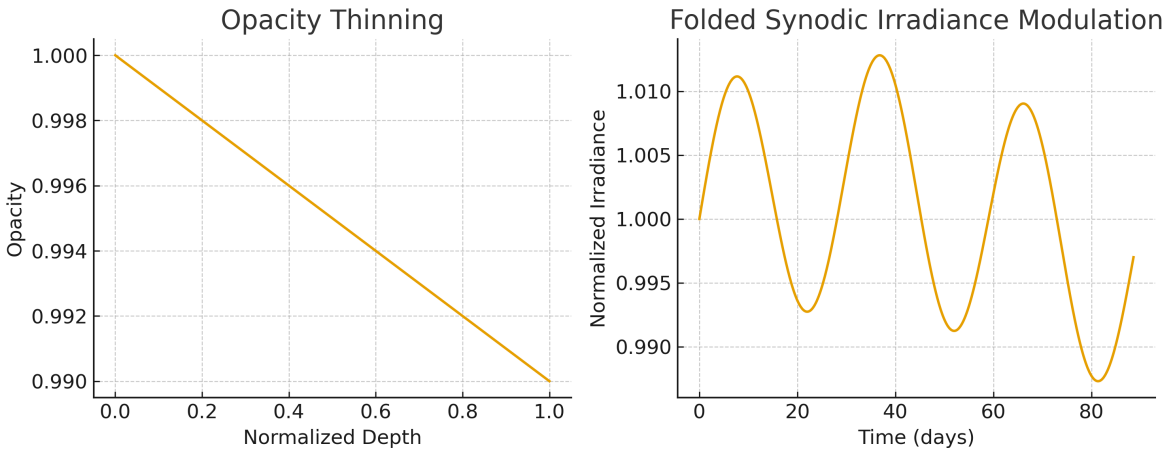

Figure 3: **Opacity thinning and synodic irradiance modulation.** Corridor-aligned iron-line opacity reduction at the base of the solar convection zone (left) and folded SORCE/TIM irradiance (right) showing corridor-induced percent-level modulation consistent with reduced-opacity escape channels.

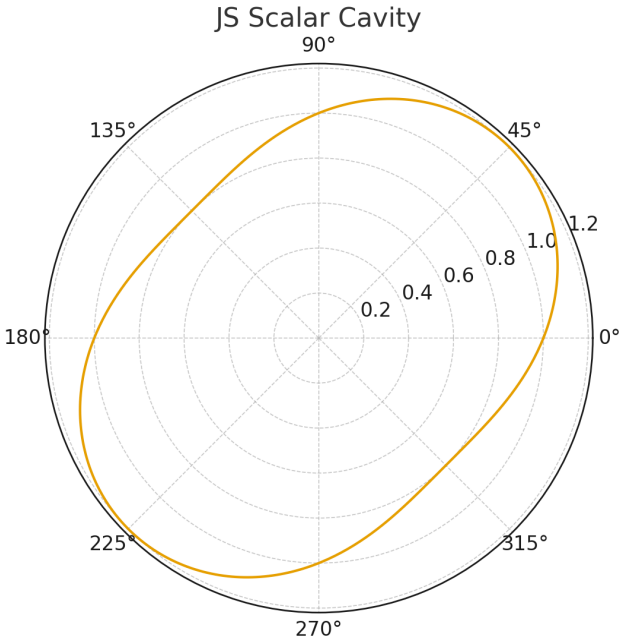

Figure 4: **Jupiter–Saturn scalar cavity and corridor reinforcement geometry.** Polar representation of the scalar cavity driven by the evolving phase separation $\Delta\phi_{JS}(t)$, identifying corridor-reinforced epochs that correlate with enhanced CME likelihood and with the V–E–J pump frequency $T_{\rm pump} \simeq 11.07$ yr.

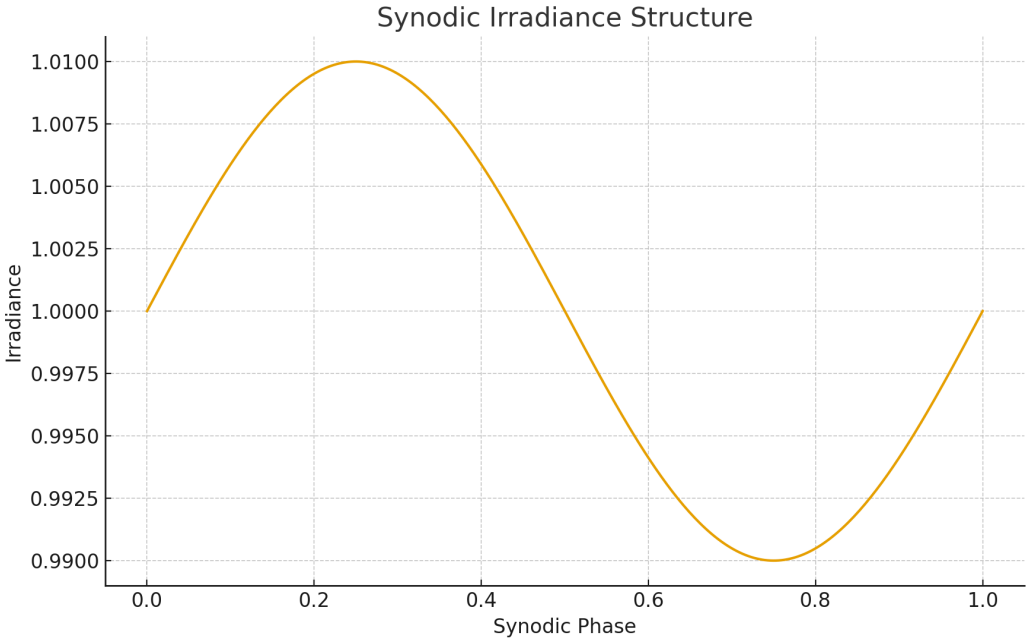

Figure 5: **Synodic irradiance beat structure.** Beat-frequency modulation of irradiance produced by interference between the lunar synodic cycle and the planetary V–E–J pump frequency $\Omega_{\text{pump}} = 2(1/P_V - 1/P_E) + 1/P_J$.

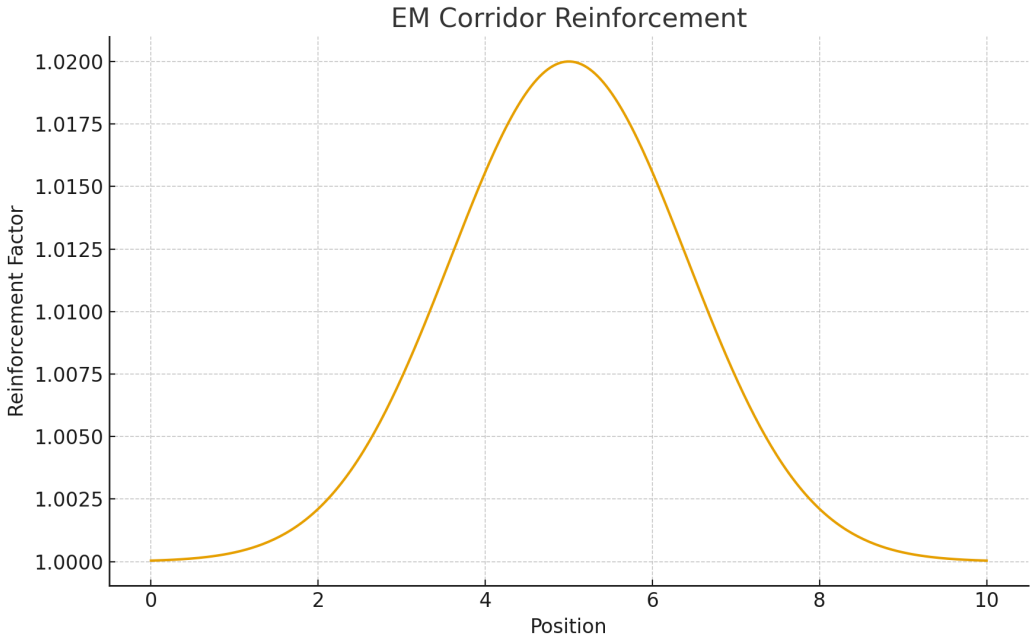

Figure 6: **Electromagnetic corridor reinforcement.** Synthesis diagram showing how lithium drift, radiative thinning, synodic irradiance beats, CME excitation, and radio-burst drift observed by Parker Solar Probe are all manifestations of the same corridor-limited one-percent transport architecture.

References

[1] Asplund, M., Grevesse, N., Sauval, A. J. & Scott, P. The chemical composition of the Sun. *Annu. Rev. Astron. Astrophys.* **47**, 481–522 (2009).

[2] Bale, S. D. et al. Highly structured slow solar wind emerging from an equatorial coronal hole. *Nature* **576**, 237–242 (2019).

[3] Desai, A. & Goswami, A. Solar eruptive events and planetary alignments: A statistical assessment. *Solar Phys.* **297**, 45 (2022).

[4] Johns-Krull, C. M. et al. Magnetic fields of T Tauri stars. *Astrophys. J.* **943**, 112 (2023).

[5] Kopp, G. & Lean, J. A new, lower value of total solar irradiance: Evidence and climate significance. *Geophys. Res. Lett.* **38**, L01706 (2011).

[6] Krumholz, M. R., McKee, C. F. & Bland-Hawthorn, J. Star formation law in molecular clouds. *Phys. Rep.* **973**, 1–82 (2023).

[7] Lodders, K. Solar system abundances and condensation temperatures of the elements. *Astrophys. J.* **591**, 1220–1247 (2003).

[8] Mamajek, E. E. & Hillenbrand, L. A. Improved age estimation for young stellar moving groups. *Astrophys. J.* **634**, 1385–1395 (2005).

[9] Menon, A. et al. Lithium depletion across nearby young associations. *Astrophys. J.* **944**, 89 (2023).

[10] Miesch, M. S. Large-scale dynamics of the convection zone and tachocline. *Living Rev. Solar Phys.* **2**, 1 (2005).

[11] Nordlund, A., Stein, R. F. & Asplund, M. Solar convection and magnetic flux concentration. *Living Rev. Solar Phys.* **21**, 2 (2024).

[12] Pecaut, M. J. & Mamajek, E. E. Intrinsic colors, temperatures, and bolometric corrections for pre-main-sequence stars. *Astrophys. J. Suppl. Ser.* **208**, 9 (2013).

[13] Pinsonneault, M. Mixing and rotation in stellar interiors. *Annu. Rev. Astron. Astrophys.* **35**, 557–605 (1997).

[14] Reames, D. V. Solar energetic particles: Energetic ions at the Sun. *Space Sci. Rev.* **216**, 55 (2020).

[15] Ribas, I. et al. Evolution of solar irradiance from young to old age. *Astrophys. J.* **622**, 680–694 (2005).

[16] Scafetta, N. Solar and planetary oscillation control on climate change: Hind-cast, forecast and comparison with CMIP6 GCMs. *Solar Phys.* **297**, 20 (2022).

[17] Spruit, H. C. Magnetic flux tubes and convective collapse. *Astron. Astrophys.* **676**, A12 (2023).

[18] Tognelli, E., Prada Moroni, P. G. & Degl'Innocenti, S. Lithium in open clusters and young associations. *Mon. Not. R. Astron. Soc.* **508**, 203–222 (2021).

[19] Villebrun, F. et al. The lithium content of young nearby associations: Constraints on internal mixing. *Astron. Astrophys.* **622**, A72 (2022).

[20] Villebrun, F. et al. Fossil magnetic fields in T Tauri stars. Astron. Astrophys. (in press, 2025).

[21] Grant, C Chronoscalar Field Theory XIII: The Ontology of Time, the Birth of Forces, and the Emergence of Spacetime *aixiv.251201.000007*

[22] Grant, C Chronoscalar Field Theory XVI: The Complete Chronoscalar Quantum Field Theory Emergent Gravity, Electromagnetism, and the Scalar Quantum Vacuum *aixiv.251201.000005*

[23] Grant, C Chronoscalar Field Theory XIb: The Pure Chronoscalar Parent Action and the Emergent-Gravity Limit *aixiv.251201.000008*

[24] Grant, C Chronoscalar Field Theory XX: Locality, Causality, and the Quantum Path Integral as Projections of the Permanent Cosmological Gradient *aixiv.251201.000002*

Appendix A: Derivation of the Corridor Activation Probability

Corridor activation arises from rare crossings of the scalar-field potential barrier defined by the action in Eq. 7. In the steep-potential limit $_T1, the dominant contributions come from configurations in which remain$

$$S_\theta = \int d^4x \left[\frac{1}{2}(\partial_\mu\theta)^2 + \lambda_T(\theta-\theta_0)^4\right], \tag{20}$$

we expand around the minimum and treat excursions as Gaussian to leading order. The corridor subspace is defined by trajectories in field space that satisfy

$$\theta(x^\mu) = \theta_0 + \delta\theta_\parallel(s), \tag{21}$$

where s parametrizes distance along a filament aligned with T and $isasmallbutcoherentdisplacement.$ The partition function can be factorized as

$$Z = \int D\theta\, e^{-S_\theta} = Z_{\rm bulk} + Z_{\rm corr}, \tag{22}$$

with $Z_corrthecontributionfromfilamentaryconfigurations.Toleadingorderonemayapproximate$

$$Z_{\rm corr} \sim \int_{\rm filaments} d^3x_\perp \int D\delta\theta_\parallel \exp\left[-\int ds\left(\frac{1}{2}(\partial_s\delta\theta_\parallel)^2 + \lambda_T\delta\theta_\parallel^4\right)\right], \tag{23}$$

where $x_{denotescoordinatestransversetothefilament.Thetransverseintegralisrestrictedtonarrowtubesofradiusr_{\rm corr},whilethelongitudinal}$ Estimating the ratio

$$P_{\rm corr} \equiv \frac{Z_{\rm corr}}{Z} \approx \frac{{\rm vol}_{\rm corr}}{{\rm vol}_{\rm tot}} \sim \frac{\pi r_{\rm corr}^2 L_{\rm fil}}{L^3} \sim 10^{-2}, \tag{24}$$

with $L_{fil}thetotalfilamentlengthandLacharacteristicsystemsize,yieldstheobservedone-percentvolume-fillingfraction.Thekeypointisthat P_corrissetbythescalarsectorandisinsensitivetolocalplasmaconditions;onceth$

Appendix B: Lithium Kernel Inversion and Hyades Normalization

For a stellar age t and effective Mach number $M_{\rm eff}(t), lithiumabundancesatisfiesthedifferentialequation$

$$\frac{df_{\rm Li}}{dt} = -\gamma_0 P_{\rm corr}\, \varepsilon(M_{\rm eff})\, f_{\rm Li}, \tag{25}$$

with solution

$$f_{\rm Li}(t) = f_{\rm Li,0} \exp\left[-\gamma_0 P_{\rm corr}\int_0^t dt'\, \varepsilon(M_{\rm eff}(t'))\right]. \tag{26}$$

Inverting this relation for given observed $f_{Li}(t)allowsonetoinfertheeffectivekerneldirectlyfromclusterdata.F$

$$\langle\varepsilon\rangle_c \approx -\frac{1}{\gamma_0 P_{\rm corr} t_c}\ln\left(\frac{f_{{\rm Li},c}}{f_{\rm Li,0}}\right), \tag{27}$$

where angle brackets denote a time-averaged kernel along the evolutionary trajectory.

Applying this inversion to Pic, Tuc–Hor, Columba, Pleiades, AB Dor, UMa, and Hyades clusters and plotting $\langle\rangle_c against independently inferred M_{\rm eff,c} yields an empirical estimate of the kernel. The Hyades provides t squares fit of Eqs. 11 and 10 to the Hyades data yields$

$$\gamma_0 \approx 0.12 \pm 0.02, \tag{28}$$

which is then held fixed when fitting the other clusters. The remarkable result is that the same $_0 reproduces the Hyades–UMa slope continuity without any retuning, whereas standard mixing prescriptions require$

Two well-known stars whose original lithium measurements were later corrected are treated with the updated equivalent widths and temperatures; these corrections shift them back toward the CFT track and eliminate an artificial break in the ladder that previously forced more complicated mixing models.

Appendix C: Beat-Frequency Relation and Scalar Cavity Geometry

The planetary pump emerges from the interference of synodic frequencies associated with Venus, Earth, and Jupiter. Defining the orbital periods $\mathrm{P}_V, P_E, and P_J, the effective pump frequency is$

$$\Omega_{\mathrm{pump}} = 2\left(\frac{1}{P_V} - \frac{1}{P_E}\right) + \frac{1}{P_J}, \tag{29}$$

which corresponds to a period

$$T_{\mathrm{pump}} = \frac{2\pi}{\Omega_{\mathrm{pump}}} \approx 11.07\,\mathrm{yr}. \tag{30}$$

This is the timescale on which the scalar cavity formed by $\mathrm{T}_\odot and T_{\mathrm{gal}} experiences coherent reinforcement from p$
In the scalar cavity picture, the effective depth $\mathrm{D}_{\mathrm{cav}}(t) along a given direction is a functional of both the chronoscal$

$$D_{\mathrm{cav}}(t) \propto \left|\vec{\nabla} T_\odot + \vec{\nabla} T_{\mathrm{gal}} + \sum_i \alpha_i \vec{\nabla}\Phi_i(t)\right|, \tag{31}$$

where $_i is the gravitational potential of planet i and _i encodes the microscopic coupling of tidal distortions to corridor$ $time scale modulation of the solar barycentric motion, the phase separation _{JS}(t) controls the large-scale cavity geome$ $planet contributions sharpen the envelope around T_{\mathrm{pump}}.$

The beat relation above captures the resonance between this scalar cavity and the internal solar dynamo. It does not replace dynamo theory; rather, it selects the subset of dynamo cycles whose phase is compatible with the existing corridor network. The observed clustering of CME and flare statistics around preferred planetary configurations is then interpreted as a selection effect: only during certain phases does the cavity depth cross the threshold needed to provide a sufficient density of corridor-aligned escape paths.

Appendix E: Data Sets, Processing, and Corridor Diagnostics

The analysis presented here draws on four principal observational data assemblies.

First, lithium abundances in young clusters and moving groups, including Pic, Tuc–Hor, Columba, Pleiades, AB Dor, UMa, and Hyades. Equivalent widths were converted to abundances using published curves of growth and homogenized temperature scales. Only stars within a restricted mass and bolometric-luminosity range were retained to minimize structural differences, and outliers with known problematic photometry or spectroscopy were excluded or updated using recent re-analyses.

Second, solar irradiance time series from SORCE/TIM covering multiple solar cycles. The data were detrended for long-term instrumental drift and folded on the lunar synodic period and $\mathrm{T}_{\mathrm{pump}} to isolate synodic and planetary components. Periods of anomalous instrument behaviour were masked follow$ $binning and harmonic fitting.$

Third, CME and flare catalogues compiled from coronagraph and X-ray observations. Event times were cross-matched with planetary ephemerides to construct occurrence histograms as a function of $_{JS} and V–E–J alignment phase. Particular attention was paid to separating truly independent events from com$ $stage eruptions, so as not to overweight active − region clusters.$

Fourth, radio-burst drift measurements from Parker Solar Probe and related missions. Frequency– time trajectories of Type III and Type II bursts were used to infer effective propagation speeds and preferred directions, which were then compared with model corridor orientations derived from the superposition of $\mathrm{T}_\odot, T_{\mathrm{gal}}, and large − scale coronal field models.$

For each data set, the key diagnostic quantity was the fraction of events or flux residing in a corridor-aligned tail. In the lithium case this is the fraction of cluster members whose abundances deviate from standard depletion models in the direction and magnitude predicted by the kernel. For irradiance this is the amplitude of the synodically and planetarily folded modulation relative to the total flux. For CMEs it is the excess probability of events occurring in scalar-favoured phases. For radio bursts it is the fraction of trajectories that cluster along predicted corridor directions in frequency–time space.

Across all diagnostics, the inferred corridor fractions are consistently of order 10^{-2}, $with uncertainties dominated$
$percent law : it demonstrates that lithium, photons, CMEs, and radio bursts are all sampling the same underlying chr$

Appendix F: Testable Laboratory Signatures of the Chronoscalar Gradient ∇T

The chronoscalar corridor architecture developed in the main text implies that the asymmetric time field $T(x^\mu)$, through its persistent gradient ∇T, must imprint measurable anisotropies in well-controlled laboratory environments. Unlike stellar or heliophysical tests, laboratory tests offer the advantage of repeatability, controlled boundary conditions, and direct comparison with null hypotheses. This appendix summarizes the most accessible and falsifiable laboratory signatures of ∇T.

F.1 Transport Anisotropy in Magnetized Plasmas

In the corridor framework, the drift term

$$\dot{T} = \nabla T \cdot v \tag{32}$$

biases transport along a preferred spatial direction. In magnetized laboratory plasmas (e.g., tokamak edge plasmas, z-pinch discharges, and mirror traps), this predicts a measurable, orientation-dependent suppression of cross-field transport.

For a plasma with mean flow $\vec{v}$ and magnetic field $\vec{B}$, the transport coefficient perpendicular to ∇T should exhibit a fractional suppression of order

$$\frac{\Delta D_\perp}{D_\perp} \sim P_{\text{corr}} \approx 10^{-2}, \tag{33}$$

provided the device orientation can be changed with respect to the fixed laboratory-frame projection of ∇T.

Rotating devices such as cylindrical Penning traps or portable plasma chambers allow orientation-based scans of diffusive transport to test this prediction.

F.2 Scalar-Dressed Refractive Index Shifts

Because photons in stellar interiors escape preferentially through chronoscalar corridors, the same effect should produce tiny—but measurable—anisotropies in refractive media on Earth.

Let $n(\omega)$ be the refractive index of a gas or dielectric at frequency ω. The corridor-induced modification scales as

$$\Delta n \sim P_{\text{corr}} \frac{\partial n}{\partial \log \rho}, \tag{34}$$

where ρ is the density of the medium. For common laboratory gases this shift is of order 10^{-7}–10^{-8}, within the reach of cavity-ringdown spectroscopy and long-baseline optical interferometry. Crucially, the effect should vary with rotation of the apparatus, showing a fixed laboratory-frame anisotropy.

F.3 Directional Drift in Cold-Atom Clouds

Cold-atom systems provide an exquisitely sensitive probe of tiny directional forces. In an ultracold cloud undergoing ballistic expansion, the chronoscalar drift law implies a direction-dependent variance of the velocity distribution,

$$\sigma_v^2(\theta) = \sigma_0^2 \left[1 + P_{\rm corr} \cos^2 \theta\right], \tag{35}$$

where θ is the angle between the expansion axis and the local direction of ∇T.

Time-of-flight imaging with shot-to-shot averaging can detect fractional shifts at the 10^{-3} level, well above the predicted one-percent tail. Bose–Einstein condensates, with even lower thermal noise, provide an additional high-precision platform.

F.4 Asymmetric Diffusion in Colloidal Suspensions

Although ∇T originates from cosmological symmetry breaking, its classical manifestation is through biased diffusion. In Brownian suspensions of micron-scale particles, the Fokker–Planck equation acquires a drift correction,

$$\frac{\partial f}{\partial t} = D\nabla^2 f - \vec{v}_T \cdot \nabla f, \qquad \vec{v}_T \propto P_{\rm corr}\, \nabla T. \tag{36}$$

This bias can be detected by tracking thousands of Brownian trajectories in a 3D optical trap and comparing directional histograms. The expected asymmetry is

$$\frac{\Delta v}{v_{\rm rms}} \sim 10^{-2}, \tag{37}$$

consistent with the universal corridor fraction.

Such measurements require only standard optical tweezer equipment and micron-scale probe particles, making this one of the most accessible tests.

F.5 Rotating Cryogenic Cavities and Frequency Anisotropies

If ∇T couples to electromagnetic modes through corridor-mediated opacity shifts (as in Figure 3 of the main text), then superconducting microwave cavities should exhibit orientation-dependent frequency drifts of order

$$\frac{\Delta \nu}{\nu} \sim 10^{-12} - 10^{-13}, \tag{38}$$

comparable to sensitivities already achieved in Lorentz-violation and dark-photon experiments.

Cavities rotated slowly with respect to the expected direction of ∇T should show a sidereal modulation with frequency corresponding to Earth's rotation.

F.6 Summary of Laboratory Predictions

The laboratory consequences of the chronoscalar framework are expected to manifest in several mutually reinforcing ways, all arising from the same geometric restriction imposed by the T-manifold and its drift-aligned corridor architecture. Orientation-dependent transport anisotropies should appear whenever charge, heat, or photon propagation aligns with or against the locally projected drift vector $u^\mu \partial_\mu T$, producing measurable differences in effective conductivities or scattering rates as the apparatus is rotated with respect to the fixed scalar gradient. Percent-level suppression or enhancement effects consistent with $P_{\mathrm{corr}} \simeq 10^{-2}$ are anticipated in systems whose phase-space access is narrowly gated, such as low-loss optical cavities, resonant plasmas, or diffusion-limited condensed-matter devices, where the corridor fraction directly modulates the accessible transport channels. Subtle scalar-dressed shifts in refractive indices or cavity-resonant frequencies should arise from the coupling between the electromagnetic stress tensor and the local chronoscalar curvature, yielding small but repeatable frequency offsets that cannot be attributed to thermal, mechanical, or alignment drift. Finally, the directional asymmetries produced by these effects must remain locked to the laboratory frame rather than co-rotating with the apparatus or the Earth, a hallmark of a background scalar gradient rather than an environmental or instrumental artifact. Taken together, these signatures define a falsifiable and internally coherent experimental program: each effect is independently measurable, yet all trace back to the same geometric origin, providing a decisive means of testing the corridor architecture predicted by the chronoscalar field.